Spatially resolved ballistic optoelectronic transport measured by quantized photocurrent spectroscopy

Supporting Information

Klaus-Dieter Hof,[1] Franz J. Kaiser,[2] Markus Stallhofer,[3] Dieter Schuh,[4] Werner Wegscheider,[5] Peter Hänggi,[2] Sigmund Kohler, [2,6] Jorg P. Kotthaus,[1] and Alexander W. Holleitner[3]*

1 Fakultät für Physik and Center for NanoScience (CeNS), Ludwig-Maximilians-Universität, Geschwister-Scholl-Platz 1, D-80539 München, Germany

2 Institut für Physik, Universität Augsburg, Universitätsstraße 1, D-86135 Augsburg, Germany

3 Walter Schottky Institut and Physik Department, Technische Universität München, Am Coulombwall 3, D-85748 Garching, Germany

4 Institut für Experimentelle und Angewandte Physik, Universität Regensburg, D-93040 Regensburg, Germany

5 Laboratorium für Festkörperphysik, HPF E 7, ETH Zürich, Schafmattstr. 16, 8093 Zürich, Switzerland

6 Instituto de Ciencia de Materiales de Madrid, CSIC, E-28049 Madrid, Spain

* Corresponding author: Alexander W. Holleitner e-mail: holleitner@wsi.tum.de

1. Heterostructure

The heterostructure used in this experiment is grown by molecular beam epitaxy (MBE) on a GaAs substrate. In growth order, the layers are: 1.5 μm $Al_{0.3}Ga_{0.7}As$, 100 nm $Al_{0.3}Ga_{0.7}As$, 25 nm GaAs, 60 nm $Al_{0.3}Ga_{0.7}As$, 16.5 nm AlGaAs:Si, 14 nm $Al_{0.3}Ga_{0.7}As$, and 5 nm GaAs. The two-dimensional electron gas (2DEG) resides in the 25 nm GaAs layer, with mobility $\mu = 1.74 \times 10^6$ cm^2/Vs and density $n = 2.75 \times 10^{11} cm^{-2}$ at 4.2 K. These values correspond to an electronic mean free path $l_{mfp} = 15.1$ μm, a Fermi wavevector $k_{Fermi} = 1.31 \times 10^6$ cm^{-1} and a Fermi energy $E_{Fermi} = 9.83$ meV. We compute the energy difference between the first and second subband of the quantum well to be $E_{2ndSUB} - E_{1stSUB.} = 21.07$ meV. The QPCs are patterned by e-beam lithography and a shallow-etch technique using $H_2SO_4 : H_2O_2 : H_2O = 1 : 3 : 100$ for ~ 40-50 s. The topgates are fabricated by Ti/Au (5 nm / 110 nm).

2. Experimental Scheme:

The optoelectronic circuits are mounted both in a vacuum chamber at the bottom of a He^4 cryostat and in a flow-cryostat. In both cases, a three-dimensional positioning stage with nanometer precision moves a laser spot across the circuit. No feedback was used to stabilize the position of the laser spot relative to the QPC. The laser spot size is 2.6 μm. The application of a positive voltage V_G between the topgates and the 2DEG opens the electron channel in the QPCs. All conductance and photocurrent measurements are measured between two ohmic contacts to the 2DEG.

Electrical conductance measurements (Figure 1b of the main article) are performed with a lock-in amplifier at 117.1 Hz with a voltage-biased configuration with $V_{rms} = 17.3$ μV. The optical beam induced current (OBIC) measurements (Figures 2b and 2c, 3, and 5 of the main article) are performed at 76 MHz utilizing the trigger frequency of a mode-locked titanium:sapphire laser and a lock-in amplifier. For further control measurements, photocurrent and -conductance measurements are performed at dc and a trigger frequency in the range of 100 Hz to 100 MHz (see section 5 of the Supporting

Information). The titanium:sapphire laser produces pulses of 150 fs and an energetic FWHM ~ 12 meV, and it is continuously tunable in the photon energy range 1.241 eV – 1.773 eV.

The FWHM is smaller than $E_{2ndSUB} - E_{1stSUB} = 21.07$ meV, such that at resonant excitation, only the first subband of the quantum well is optically excited. We compute the threshold excess energy for plasmon emission Δ_c to be 20.3 meV above E_{Fermi}.[1,2,3] The limit for LO-phonon emission is ~36 meV. Hereby, we conclude that plasma and phonon scattering processes play only a minor part in the OBIC.

3. Fitting parameters in Figure 3a:

The off-set values A_{OFFSET} of the fitting functions in Figure 3a are (1.08 ± 0.13) nA, (1.65 ± 0.12) nA, (1.80 ± 0.21) nA, (2.00 ± 0.07) nA, (1.60 ± 0.29) nA, (1.58 ± 0.18) nA, and (1.29 ± 0.25) nA for P_{LASER}: 15 nW, 50 nW, 125 nW, 250 nW, 500 nW, 1 μW, and 1.5 μW. The errors are fitting errors, as they are for δ_{PHOTO} in Figure 3b. We interpret the values to vary because of slight changes of temperature and electromagnetic noise in the laboratory.

In the following, the fitted amplitude of A_{OBIC} vs. P_{LASER} is discussed. To this end, the fitted values of A_{OBIC} as in Figure 3a of the main article are plotted vs. P_{Laser} in the Supporting Figure I. Within the experimental error, we find that the fitted values A_{FIT} are proportional to P_{Laser}^{x}, with x = 0.53 ± 0.09. If there was no scattering, one would expect the photo-generated current to go linearly with excitation power. The found sub-linear dependence means that some of the photo-generated electrons have scattered before they reach the quantum wire. This finding is consistent with the interpretation in the main manuscript that the photo-generated electrons are assumed to scatter at a few electrons during $\tau_{transit}$ before they reach the QPC, and, that the energy distribution of photo-generated electrons approaching the QPC can be estimated to be a combination of a Gaussian and a Maxwell-Boltzmann distribution.

We note that the dynamical electron-electron screening in semiconductors has been explored before in several ultrafast optical experiments.[4] In particular, the dependence of the dynamical screening was

discussed to follow a power law in terms of $n^{-1/D}$, where *D* represents the dimension of the electron systems.[5,6,7] We tentatively interpret our findings to be consistent with this formula.

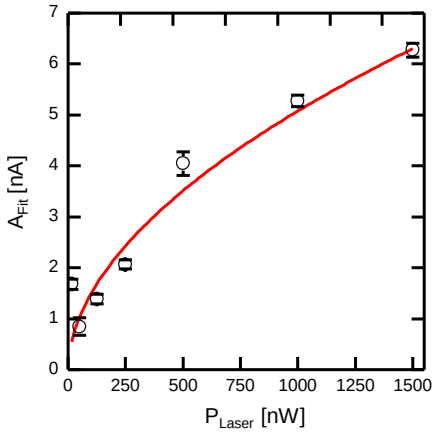

Supporting Figure I. Laser power dependence of the fitted amplitudes A_{FIT} taken from Figure 3a of the main manuscript. The red line is a fit as discussed in section 3 of the Supporting Information.

4. Monte Carlo Simulation:

In the Monte Carlo simulation, the detection probability $w(x, y)$ is sampled from 10000 runs for each starting point (x, y) with a grid size of 1×1 μm^2 in the optoelectronic circuit of Fig. 2a. Since we consider electron relaxation by the path-length dependent factor $\exp(-d/l_{mfp})$ with l_{mfp}=15 μm, the initial kinetic energy is not relevant. At position B and for experimental parameters as in Figure 2c of the main article, we compute w to be in the range of 0.01 to 0.1. In a simplifying approach, the resulting ballistic classical electron current through the QPC can be estimated to be $I_{Estimate} = w \ e \ (1 - R) \ e^{-\beta D} \ (1-e^{\alpha W}) \ P_{LASER} / E_{Photon}$, with the reflection coefficient $R \sim 0.3$ of the heterostructure, e the electron charge, D = 95.5 nm the distance of the quantum well from the surface of the heterostructure, W = 25 nm the width of the quantum well, and $\alpha \sim 10^4$ cm^{-1} ($\beta \sim 0$) the absorption coefficient of GaAs (AlGaAs) at E_{Photon} = 1.552 eV and low temperature. At P_{LASER} = 1 μW, $I_{Estimate}$ can be estimated to be in the range of ~0.1 to 1 nA, which is consistent with the order of magnitude of A_{OBIC} in Figure 3a. We note that this simple estimate does not include any electron-electron scattering as discussed in the main manuscript. The amplitude A_{OBIC} vs. P_{Laser} is discussed in section 3 of the Supporting Information.

5. Ballistic photocurrent vs. photoconductive gain effects / Trigger frequency dependence of the OBIC:

As recently demonstrated[9], photo-generated holes can give rise to a photoconductive gain effect in nanoscale semiconductor circuits at low temperatures. In this process, photo-generated electrons and holes are separated from each other due to internal electric fields at the boundaries of the samples. The holes drift to the boundaries of the circuits, where they influence the chemical potential of the 2DEG capacitively.[8] The separation of the electron-hole pairs and the recombination of the spatially separated electrons and holes occur on the milliseconds time scale[9]. A micrograph of the circuit is depicted in the Supporting Figure IIa. When the OBIC is measured at a continuous laser excitation (Supporting Figure IIb), both the ballistic photocurrent processes due to the photo-generated electrons (as discussed in the

main text) and the photoconductive gain effect caused by the photo-generated holes (as discussed in refs.[8,9]) are superimposed in the OBIC maps of the circuit. At a lock-in frequency in the kHz regime, the photoconductive gain effect dominates the OBIC. In turn, the OBIC map clearly shows the boundaries of the circuit (Supporting Figure IIc). Only at a trigger frequency in the MHz regime, the lobe structure of the ballistic photocurrent appears (Supporting Figures IId to IIf). Even at a trigger frequency of 76 MHz (Supporting Figure IIf), a reminiscent signal of the photoconductive gain effect is still detectable at the drain reservoirs; which can be explained as follows. The current-voltage amplifier is electronically attached to the drain reservoir. Hereby, the current-voltage amplifier is sensitive to changes of the chemical potential of the drain reservoir. In between the drain and the source reservoir, the QPC is placed with an impedance of ~10^4 Ω. In turn, the current-voltage amplifier is less sensitive to photon-induced current effects in the source reservoir. Most importantly, the signal of the ballistic photocurrent in the source reservoir can be detected, because the electrons ballistically propagate through the QPC into the drain reservoir, where they relax. Hereby, the quantum wire acts as an energy and momentum filter for the photo-generated electrons propagating from source to drain. Since we utilize a local laser excitation, the OBIC gives access to the energy and momentum distribution of the laser-induced current.

Generally, electrons, which are optically created in the drain reservoir, can also ballistically propagate into the source reservoir. The OBIC of such electrons can be detected at a larger laser power (see Supporting Information, Section 7).

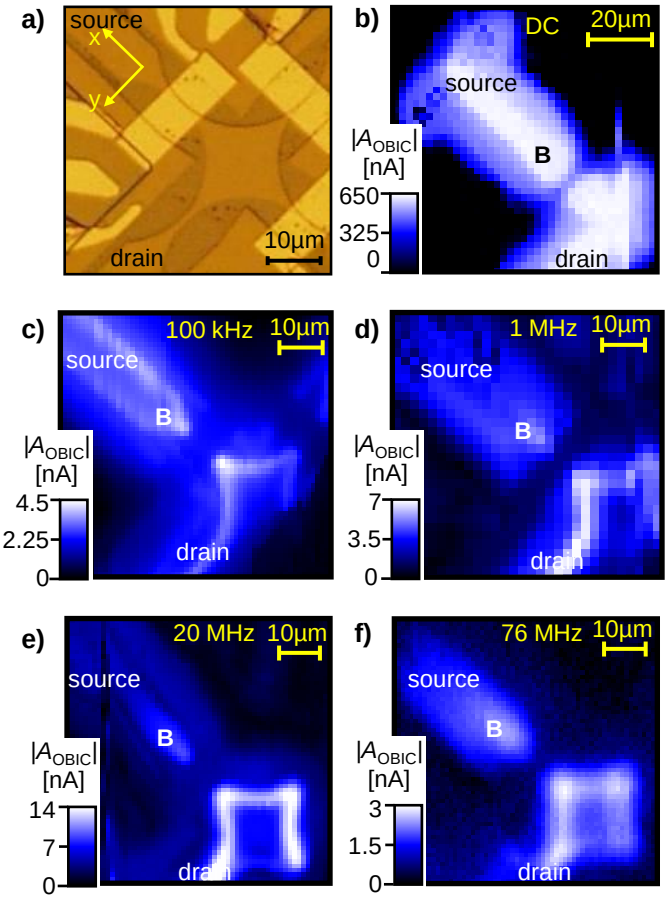

Supporting Figure II(a) Micrograph of the optoelectronic circuit, in which the source and drain configuration is depicted. The graph is tilted by +135° with respect to Figure 2a of the main article. (**b)** OBIC map of the circuit at a continuous laser excitation. (**c-f)** OBIC map of the circuit for a trigger frequency of 100 kHz, 1MHz, 5 MHz, 20 MHz, and 76 MHz at 4.2 K at V_{SD} = -2 mV, V_G = 230 mV, T = 4.2 K and P_{Laser} = 0.5 to 2 mW. For a faster trigger frequency the OBIC of the ballistic photocurrent at position B can be detected.

6. Capacitive cross-coupling between source and drain reservoirs for $E_{Photon} \leq E_{QW}$:

The photoconductive gain effect of photo-generated holes gives rise to an OBIC which is symmetric with respect to the applied bias V_{SD}.[9] For $E_{Photon} \geq E_{QW}$, the photoconductive gain effect and the photocurrent signal of the photo-generated holes are superimposed in the V_{SD}-V_G plots of the OBIC (as in Figure 5h of the main article). That is the reason, why for $V_{SD} \geq 0$ in Figure 5h of the main article, a small OBIC can be detected. The photoconductive gain effect can also be detected for E_{Photon} being slightly smaller than E_{QW}, as demonstrated in the Supporting Figure IIIa. Then, surface states at the boundary of the circuit can be optically excited.[8] In turn, a symmetric OBIC with respect to V_{SD} can be detected, as recently shown also for GaAs nanowires[10]. Without the laser excitation, one can also detect a symmetric but much smaller signal (Supporting Figure IIIb). To this end, V_G needs to be increased to a level where the Schottky barrier between the Ti/Au topgate and the GaAs substrate is almost flattened (in Supporting Figure IIIb, that happens at $V_G \sim 440$ mV). Then, a capacitive cross-coupling between the source and drain reservoirs exists, which is mediated via the metal gate.

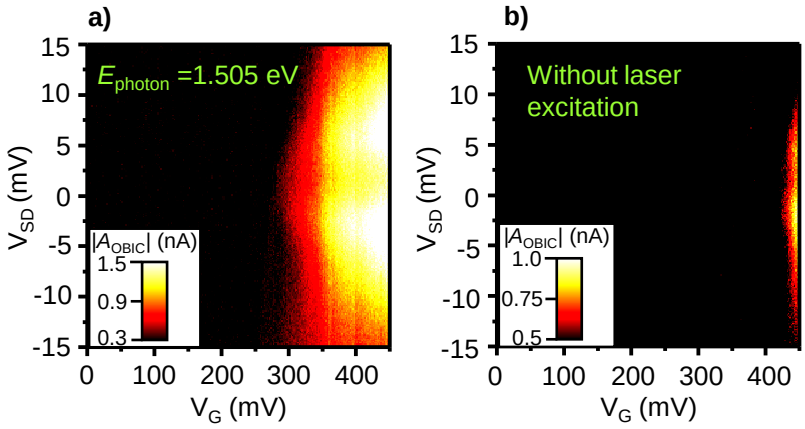

Supporting Figure III. (a) OBIC amplitude $|A_{OBIC}|$ at position B as in Figure 2c of the main article as a function of V_{SD} and V_G at 4.2 K and E_{Photon} = 1.505 eV and P_{Laser} = 50 nW. **(b)** Response of the setup with the laser being blocked, but the trigger frequency being connected to the circuit at 4.2 K.

7. Ballistic photocurrent from drain to source:

As discussed in Section 5 of the Supporting Information, our detection circuit is less sensitive to a ballistic photocurrent in the drain reservoir as in the source reservoir. At a larger laser power, however, the ballistic photocurrent of electrons created in the drain reservoir and being transmitted to the source reservoir can also be detected. The Supporting Figure IIIa defines the positions B and C. Position B equals the position B in Figure 2c of the main article. At this position B, the OBIC is asymmetric and it exhibits steps, which we interpret to stem from the one-dimensional subbands of the QPC (Supporting Figures IIIb and IIIc). At position C and a small P_{Laser}, the OBIC is symmetric with respect to the applied bias V_{SD} (Supporting Figure IIId), because then, a photoconductive gain effect dominates the OBIC (see also Section 5 of the Supporting Information)[9]. Increasing P_{Laser} up to 2 μW (Supporting Figure IIIe), the OBIC becomes asymmetric. Most importantly, the asymmetric signal is most pronounced on the positive V_{SD} side. This observation is consistent with the interpretation that now, electrons created in the drain reservoir are being transmitted to the source reservoir.

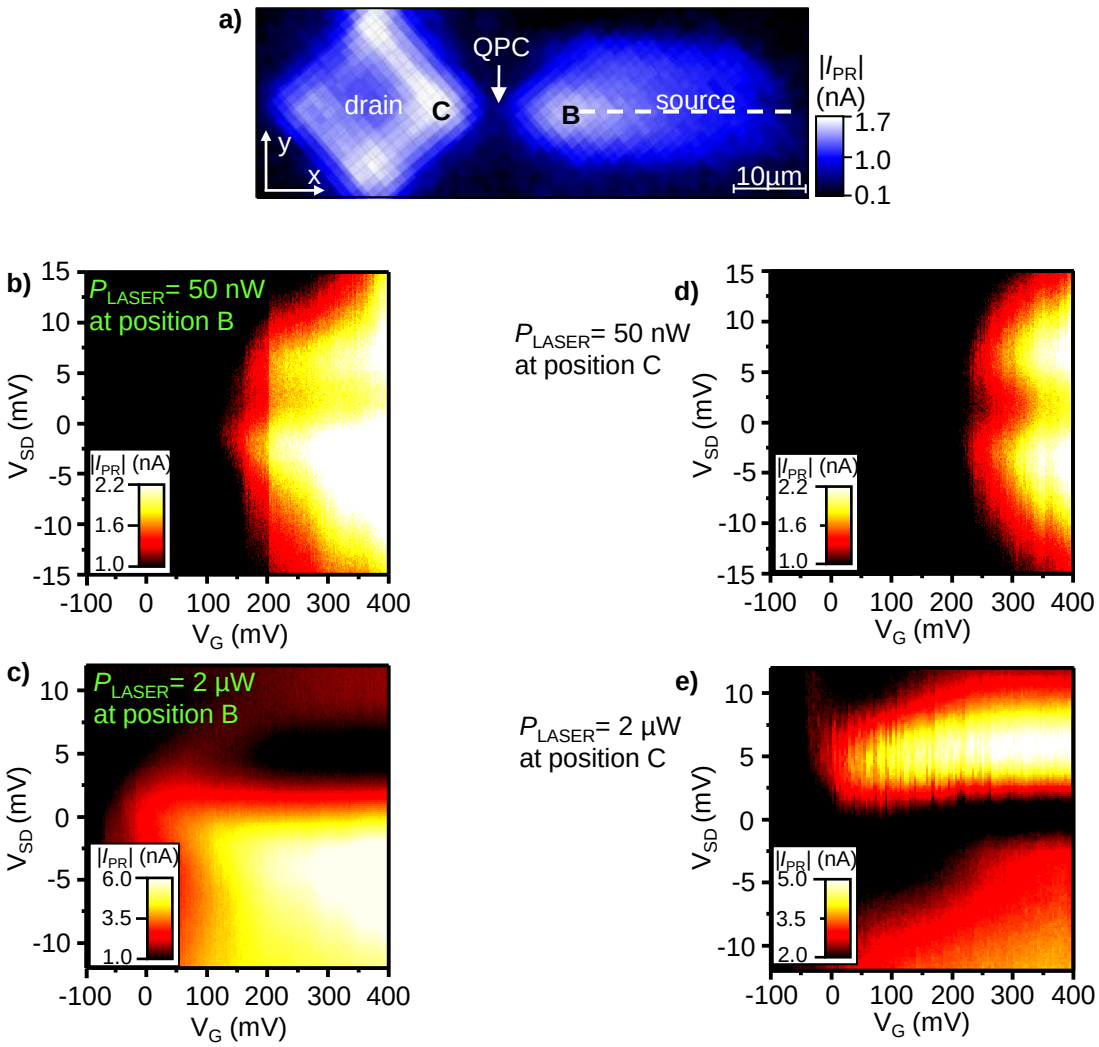

Supporting Figure III. (a) OBIC map as in Figure 2c of the main article defining the position B and C. **(b)** and **(c)** OBIC amplitude $|A_{OBIC}|$ at position B at P_{Laser} = 50 nW and 2 µW. **d** and **e**, OBIC amplitude $|A_{OBIC}|$ at position C at P_{Laser} = 50 nW and 2 µW. All measurements are performed at 4.2 K and a trigger frequency of 76 MHz.

8. Possible quasi Fermi level in the source reservoir in the direct vicinity of the QPC after photo-excitation in the source contact:

As discussed in sections 5 and 6 of the supporting information, the photoconductive gain effect of photo-generated holes gives rise to an OBIC which is symmetric with respect to the applied bias V_{SD} (see also ref. [9]). However, if the photo-excitation yields to a "new" quasi Fermi-level in the source reservoir close to the QPC, the signal of the photoconductive gain effect is expected to be shifted in V_{SD}, which can be described as follows:

$$G(V_G) = \frac{1}{V_{SD}} \int_{-\infty}^{+\infty} t(E, V_G, \Delta V_G) \cdot [f(E, \mu_S + eV_{offset}, T_S) \cdot (1 - f(E, \mu_D, T_D)) - f(E, \mu_D, T_D) \cdot (1 - f(E, \mu_S + eV_{offset}, T_S))] dE \, .$$

The parameters are defined as in ref. [9]. The term eV_{offset} describes the shift due to the possible presence of an optically induced quasi Fermi level. Experimentally, we observe that the OBIC, which is due to a photoconductive gain effect, exhibits a small shift with respect to V_{SD}. In the Supporting Figure IV, we plot the corresponding maximum shift. The experimentally obtained values are smaller than 3 meV, and they vary in a non-systematic manner for 785 nm $\leq \lambda_{\mathrm{Photon}} \leq$ 821 nm. We note that also a voltage off-set of the utilized current-voltage converter might contribute to the measured value of V_{offset}. If, however, the shift is only caused by a "new" quasi-Fermi level, the value still does not explain the suppression of the photocurrent for $V_{SD} > 4$ meV (as in Fig. 5h of the main article and other photon energies). Instead, for $V_{SD} > 4$ meV, we argue that the suppression of the photocurrent is caused by a mismatch of the energy and momentum values of the photo-generated electrons and the electron modes within the one-dimensional quantum point contact (see discussion of Fig. 5e, f, g, and h in the article).

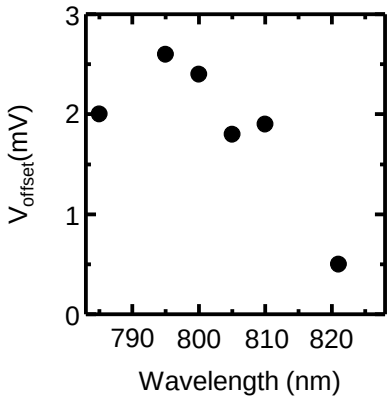

Supporting Figure IV. Bias off-set V_{offset} of the photoconductive gain effect as discussed in section 6 of the Supporting Information as a function of the photon wavelength.

References for Supporting Information:

1. Schäpers, Th.; Krüger, M.; Appenzeller, J.; Förster, A.; Lengeler, B.; Lüth, H. *Appl. Phys. Lett.* **1995**, *66*, 3603.

2. Cumming, D. R. S.; Davies, J. H. *Appl. Phys. Lett.* **1996**, *69*, 3363.

3. Wilson, T.; Gannaway, J. N.; Johnson, P. *J. of Microscopy* **1980**, *118*, no. 3, 309.

4. Shah, J. Ultrafast Spectroscopy of Semiconductors and Semiconductor Nanostructures (Springer, Berlin, 1996).

5. Bigot, J.-Y.; Portella, M.T.; Schoenlein, R.W., Cunningham, J.E.; Shank, C.V. *Phys. Rev. Lett.* **1991**, *67*, 636.

6. Becker, P.C.; Fragnito, H.L.; Brito Curz, C.H; Fork, R.L., Cunningham, J.E.; Henry, J.E.; Shank, C.V. *Phys. Rev. Lett.* **1988**, *61*, 1647.

7. Snoke, D. *Phys. Rev. B* **1994**, *50*, 11583.

8. Rossler, C.; Hof, K.-D.; Manus, S.; Ludwig, S; Kotthaus, J. P.; Simon, J.; Holleitner, A. W.; Schuh, D; Wegscheider, W. *Appl. Phys. Lett.* **2008**, *93*, 071107.

9. Hof, K.-D.; Rossler, C.; Manus, S.; Kotthaus, J. P.; Holleitner, A.W.; Schuh, D.; Wegscheider, W. *Phys. Rev. B* **2008**, *78*, 115325.

10. Thunich, S.; Prechtel, L.; Spirkoska, D.; Abstreiter, G.; Fontcuberta i Morral, A.; Holleitner, A. W. *Appl. Phys. Lett.* **2009**, *95*, 083111.